

Correction for mechanical inaccuracies in a scanning Talbot-Lau interferometer

Wolfgang Noichl, Fabio De Marco, Konstantin Willer, Theresa Urban, Manuela Frank, Rafael Schick, Bernhard Gleich, Lorenz Hehn, Alex Gustschin, Pascal Meyer, Thomas Koehler, Ingo Maack, Klaus-Jürgen Engel, Bernd Lundt, Bernhard Renger, Alexander Fingerle, Daniela Pfeiffer, Ernst Rummeny, Julia Herzen, Franz Pfeiffer

Abstract—Grating-based X-ray phase-contrast and in particular dark-field radiography are promising new imaging modalities for medical applications. Currently, the potential advantage of dark-field imaging in early-stage diagnosis of pulmonary diseases in humans is being investigated. These studies make use of a comparatively large scanning interferometer at short acquisition times, which comes at the expense of a significantly reduced mechanical stability as compared to tabletop laboratory setups. Vibrations create random fluctuations of the grating alignment, causing artifacts in the resulting images. Here, we describe a novel maximum likelihood method for estimating this motion, thereby preventing these artifacts. It is tailored to scanning setups and does not require any sample-free areas. Unlike any previously described method, it accounts for motion in between as well as during exposures.

Index Terms—Image enhancement/restoration (noise and artifact reduction), Image reconstruction - iterative methods, X-ray imaging and computed tomography

I. INTRODUCTION

In grating-based X-ray phase contrast, a periodic (reference) intensity pattern is generated in the detector plane, whose distortion is then used to calculate the projected attenuation, refraction, and small-angle scattering image of the sample. This intensity pattern may simply be the shadow of a grating,

Submitted 02-02-2021. We acknowledge financial support through the European Research Council (AdG 695045) and the DFG (Research Training Group GRK 2274). This work was carried out with the support of the Karlsruhe Nano Micro Facility (KNMF, www.kit.edu/knmf), a Helmholtz Research Infrastructure at Karlsruhe Institute of Technology (KIT).

W. Noichl, F. De Marco, K. Willer, T. Urban, M. Frank, R. Schick, B. Gleich, L. Hehn, A. Gustschin, J. Herzen, and F. Pfeiffer are with the Chair of Biomedical Physics, Department of Physics and Munich School of BioEngineering, Technical University of Munich, 85748 Garching, Germany (email: wolfgang.noichl@tum.de).

P. Meyer is with the Karlsruhe Institute of Technology, Institute of Microstructure Technology, 76344 Eggenstein-Leopoldshafen, Germany.

T. Koehler is with Philips Research, 22335 Hamburg, and TUM Institute for Advanced Study, Technical University of Munich, 85748 Garching, Germany.

I. Maack and B. Lundt are with Philips Medical Systems DMC GmbH, 22335 Hamburg, Germany.

K.-J. Engel is with Philips Research Eindhoven, 5656 AE Eindhoven, The Netherlands.

B. Renger, A. Fingerle, D. Pfeiffer, E. Rummeny, and F. Pfeiffer are with the Department of Diagnostic and Interventional Radiology, School of Medicine and Klinikum rechts der Isar, Technical University of Munich, 81675 München, Germany.

but for higher sensitivities, the Talbot effect can be utilized [1], [2], which creates an intensity pattern resembling the grating at distinct propagation distances. Resorting to the Talbot effect also has the advantage that it can be induced by a diffraction grating, which preserves more of the source's flux. The pitch of this pattern is often much smaller than the detector's resolution and thus cannot be resolved directly. In this case, an additional absorption grating is placed in front of the detector, translating this intensity pattern to an intensity modulation depending on the relative position of the gratings [3].

Standard X-ray tubes providing sufficient flux for medical imaging, however, do not feature the required spatial coherence; the intensity pattern would vanish due to focal spot blur. This limitation is circumvented by placing a third grating close to the source [4], effectively splitting it into an array of line sources. Each aperture is sufficiently small to create an interference pattern. Even though these are mutually incoherent, the distance of these apertures is chosen so that they all create the same intensity pattern, which makes the technique accessible for clinical applications.

In the past decade, this idea has been developed from proof of concept, first demonstrations of X-ray dark-field imaging [5] to various trials on animal models, human samples, and even patients [6]. Imaging of the lung has become one of the most promising candidates for future clinical application, since there is no non-invasive imaging modality available so far that can probe the lung's microstructure, and because its alveolar structure causes a large amount of coherent ultra-small angle scattering, which amounts to a strong contrast in the dark-field image. After encouraging results in *in vivo* pigs [7] and human cadavers [8], a clinical dark-field chest radiography demonstrator system has been conceived and built [9], which is also subject of this paper.

In order to achieve a field of view that is larger than the gratings currently available, the interferometer has to be moved with respect to the sample. By detuning the interferometer, sampling the interference pattern and scanning the sample is done simultaneously, moving either the sample [10] or the entire interferometer including the detector [11]. This comes at a cost: the alignment of the gratings is harder to maintain during acquisition for a moving interferometer. For thoracic imaging of patients, the scan has to be quick to avoid motion artifacts from breathing, which makes it even harder

to maintain the grating alignment.

Several methods have been proposed to remove artifacts caused by random alignment inaccuracies. A recently published method based on deep learning [12] requires repeated training whenever the flat field changes, and is built upon the assumption of a weakly scattering sample, which is not valid for our setup. Methods based on principal component analysis (PCA) [13], [14] require a fixed position of the sample with respect to the interferometer. In [15], the authors provide expressions for the artifacts resulting from a small deviation from ideal stepping, and propose a removal procedure based on the assumption that image and artifacts are uncorrelated. Because sampling in a scanning acquisition scheme is highly irregular, this approach is not compatible with scanning acquisition either. The algorithm described in [16] does not have that limitation: grating positions are estimated assuming that the correct ones yield the most smooth attenuation and dark-field images. Again, this requires an image that is entirely uncorrelated with the artifacts. In [17], this issue becomes apparent: describing an improved variant of the aforementioned algorithm, the authors note that estimated grating positions differ on whether differential-phase or dark-field images are assumed to be smooth.

For scanning setups (as opposed to phase stepping), only one procedure has been discussed so far [18]: rotation, offset and curvature of the gratings are estimated by assuming that the true grating position maximizes the correlation between reference and sample raw image. This works best in sample-free areas on the detector, which are not always available in a clinical setting due to careful collimation.

A completely different approach solely relies on a least-squares fit, extending the cost function of per-pixel phase retrieval by per-exposure parameters. While being less robust, this has the advantage that there are no additional assumptions on the image. The most popular algorithm for that is the one described in [19], which has successfully been applied to grating-based X-ray imaging [20], [21]. Unfortunately, their approach of alternating optimization for images and per-shot parameters shows very slow convergence for data acquired by scanning. An extension to more mechanical degrees of freedom has been demonstrated [22], still relying on some kind of alternating optimization. Only recently, a superior optimization scheme for the very same cost function has been suggested [23] for linear displacements in static interferometers.

In this paper, we present a novel way of mitigating vibration artifacts in a large, quickly moving scanning grating interferometer. Formulated as a maximum likelihood problem, it incorporates for the first time both motion in between as well as during exposures, which is shown to be impossible for stepping setups. Alternating optimization is replaced by a gradient descent scheme, which is both faster for scanned data sets and opens up further possibilities for optimization, like quasi-Newton methods or preconditioning.

II. METHODS

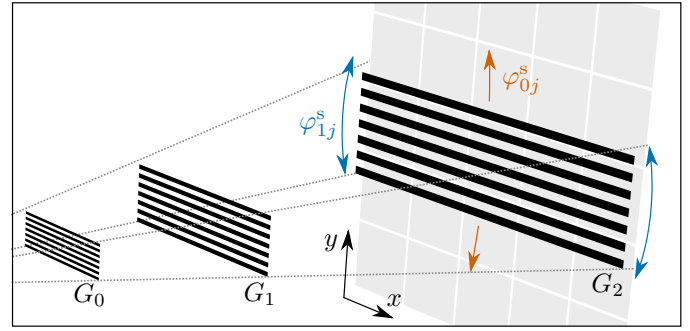


Fig. 1. Setup and origin of vibration artifacts. The setup is a Talbot-Lau interferometer, operated in scanning mode; the active area sweeps across the detector as the interferometer is rotated upward around the focal spot of the X-ray source. Without loss of generality, the third grating G_2 is subject to vibrations. If the grating itself is assumed to be rigid, two degrees of freedom are particularly notable: a “tip” movement φ_{0j}^s and a “tilt” movement φ_{1j}^s .

A. Image formation model

For a Talbot-Lau interferometer, the expectation value of the intensity measured by a single detector pixel can be approximated as [4]:

$$\bar{I} = t^f t (1 + v^f v \cos(\varphi^f + \varphi)). \quad (1)$$

Here, the interferometer itself is characterized by the so-called flat field, i.e. the mean intensity t^f , the visibility of the reference pattern v^f , and its position φ^f with respect to the analyzer grating in units of $p_2/2\pi$, where p_2 is the pitch of the analyzer grating. The influence of the sample is described by its transmittance t as well as a visibility reduction v and a shift φ of the reference pattern perpendicular to the grating lines. If one neglects propagation effects within the sample, t , v , and φ are related to projections of the sample’s attenuation coefficient μ , linear diffusion (dark-field) coefficient ϵ , and refractive index decrement δ along the beam path as follows:

$$t = \exp\left(-\int \mu(\mathbf{sn}) ds\right), \quad (2)$$

$$v = \exp\left(-c_v \int \epsilon(\mathbf{sn}) ds\right), \quad (3)$$

$$\varphi = c_\varphi \partial_g \int \delta(\mathbf{sn}) ds, \quad (4)$$

where \mathbf{n} is the unit vector from source to detector pixel, $c_v > 0$ and $c_\varphi > 0$ depend on the grating pitch and the setup geometry [24]–[26], and ∂_g denotes the partial derivative taken perpendicular to the grating lines.

B. Acquisition scheme and basic image reconstruction

In the following, we will assume a full-field detector whose position is fixed with respect to the sample¹. In order to be able to reconstruct t , v , and φ , one has to take a series of intensity measurements I_j with varying reference phases φ_j^f . In a fringe scanning scheme [10], [27], this is done by slightly detuning the interferometer such that there are moiré fringes

¹Generalization to a detector fixed with respect to the interferometer by shifting raw data and flat fields is straightforward.

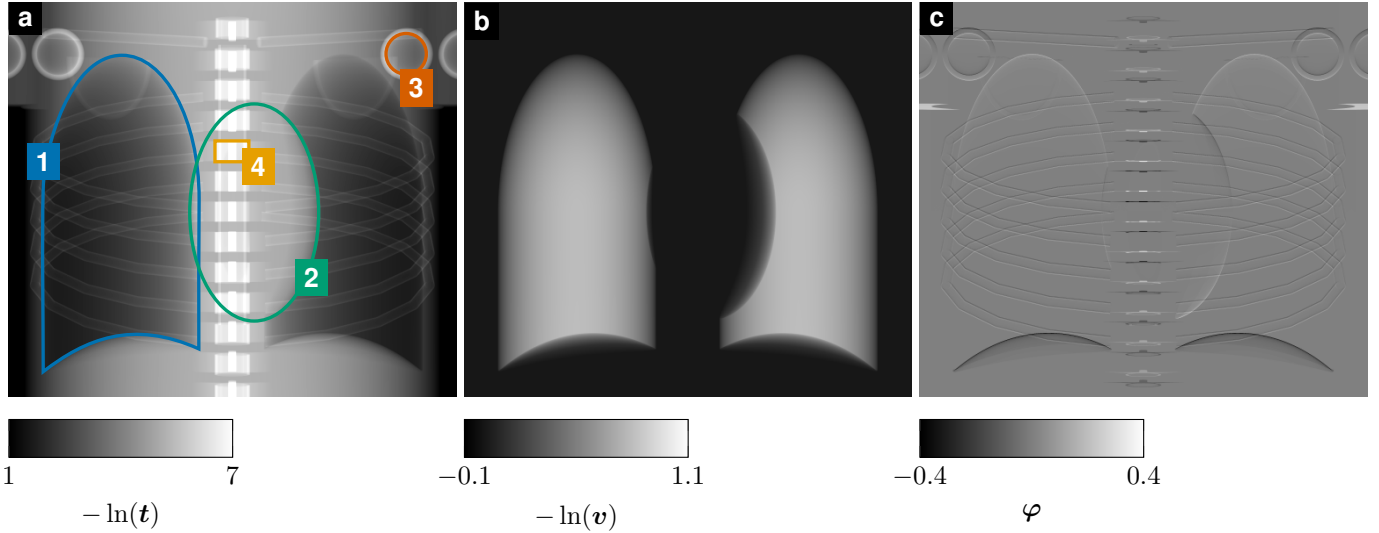


Fig. 2. Setup simulation study. Simulated (a) attenuation, (b) dark-field, (c) differential phase images, generated by a parallel-beam forward projection of an extended FORBILD phantom. The overlay in (a) indicates some of the outlines of the four distinct materials (1) lung, (2) soft tissue, (3) bone marrow, and (4) bone, whose assumed properties are listed in Table I.

perpendicular to the scanning direction. By taking acquisitions while moving the interferometer across the sample, we obtain the necessary variation of the reference phase (i.e. local grating alignment) without moving the gratings with respect to each other.

We obtain transmission t , differential phase φ , and dark-field v by solving the following least-squares problem:

$$\bar{I}_j = t_j^f t (1 + v_j^f v \cos(\varphi_j^f + \varphi)), \quad (5)$$

$$l(I_j | \bar{I}_j) = \frac{(I_j - \bar{I}_j)^2}{\sigma_j^2} \propto \frac{(I_j - \bar{I}_j)^2}{\bar{I}_j} \approx \frac{(I_j - \bar{I}_j)^2}{I_j}, \quad (6)$$

$$(\hat{t}, \hat{\varphi}, \hat{v}) = \arg \min_{t, \varphi, v} \sum_j l(I_j | \bar{I}_j). \quad (7)$$

Here, we use a data-weighted least-squares model l to approximate the log-likelihood that arises from photon shot noise (variance σ_j^2), neglecting electronic noise. The optimization problem (7) can be solved directly; for an X-ray grating interferometer, this has been described first in [28]. By a change of variables, we can reformulate (5) as a linear equation,

$$\begin{aligned} \bar{I}_j &= t_j^f t (1 + v_j^f v \cos \varphi_j^f \cos \varphi - v_j^f v \sin \varphi_j^f \sin \varphi) \\ &=: t_j^f t + t_j^f v_j^f \cos \varphi_j^f c + t_j^f v_j^f \sin \varphi_j^f s. \end{aligned} \quad (8)$$

The resulting linear least squares problem,

$$(\hat{t}, \hat{c}, \hat{s}) = \arg \min_{t, c, s} \sum_j l(I_j | \bar{I}_j), \quad (9)$$

can be solved directly by standard techniques from linear algebra, such as LDL^T Cholesky decomposition. Then, the visibility reduction and the differential phase are given by:

$$\hat{v} = \frac{1}{t} \sqrt{\hat{c}^2 + \hat{s}^2}, \quad \hat{\varphi} = \text{atan2}(-\hat{s}, \hat{c}). \quad (10)$$

C. A model for mechanical vibrations

Experimentally, we observe “tip” and “tilt” vibrations of the interferometer, whereas the gratings themselves are rigid, see Fig. 1. Equivalently, these vibrations can be described as a random displacement of the third grating G_2 : For the j th exposure, the grating is shifted perpendicular to the grating lines by φ_{0j}^s as well as rotated around the optical axis by φ_{1j}^s . For small angles and taking the translational symmetry of the gratings into account, this rotation is equivalent to a local displacement of the third grating, which is proportional to the location’s distance to the center of rotation, measured along the grating lines. Accounting only for motion between exposures results in the following model,

$$\bar{I}_{ij} = t_{ij}^f t_i (1 + v_{ij}^f v_i \cos(\varphi_{ij}^f + \varphi_{0j}^s + x_i \varphi_{1j}^s + \varphi_i)), \quad (11)$$

x_i being the x coordinate of the i th pixel. The coordinate system is chosen so that x_i of a pixel from the left/right edge of the detector is ± 1 .

Furthermore, motion may also happen during one exposure lasting over a time T . We obtain

$$\bar{I}_{ij} = \frac{1}{T} \int_{-T/2}^{T/2} t_{ij}^f t_i (1 + v_{ij}^f v_i \cos \alpha_{ij}(\tau)) d\tau \quad (12)$$

$$= t_{ij}^f t_i \left(1 + v_{ij}^f v_i \cdot \frac{1}{T} \int_{-T/2}^{T/2} \cos \alpha_{ij}(\tau) d\tau \right) \quad (13)$$

where

$$\alpha_{ij}(\tau) := \varphi_{ij}^f + \varphi_{0j}^s(\tau) + x_i \varphi_{1j}^s(\tau) + \varphi_i. \quad (14)$$

Taking only uniform movement into account,

$$\alpha_{ij}(\tau) = \alpha_{ij} + \dot{\alpha}_{ij} \cdot \tau, \quad (15)$$

this leads to a visibility reduction,

$$\frac{1}{T} \int_{-T/2}^{T/2} \cos(\alpha_{ij} + \dot{\alpha}_{ij} \tau) d\tau = \text{sinc}\left(\frac{\dot{\alpha}_{ij} T}{2}\right) \cos \alpha_{ij}, \quad (16)$$

where $\text{sinc } x := (\sin x)/x$. If the grating displacement $\dot{\alpha}_{ij}T$ happening *during* one exposure is sufficiently small, we can make the following approximation:

$$\begin{aligned} \text{sinc}\left(\frac{\dot{\alpha}_{ij}T}{2}\right) &\approx 1 - \frac{1}{6}\left(\frac{\dot{\alpha}_{ij}T}{2}\right)^2 \\ &= 1 - \frac{T^2}{24}(\dot{\varphi}_{0j}^s + x_i\dot{\varphi}_{1j}^s)^2 \\ &=: v_{0j}^s + x_i v_{1j}^s + x_i^2 v_{2j}^s, \end{aligned} \quad (17)$$

where v_0^s, v_1^s, v_2^s denote the motion-induced visibility reduction, grouped by its degree in x :

$$\begin{aligned} v_{0j}^s &= 1 - \frac{(T\dot{\varphi}_{0j}^s)^2}{24}, & v_{1j}^s &= -\frac{T^2\dot{\varphi}_{0j}^s\dot{\varphi}_{1j}^s}{12}, \\ v_{2j}^s &= -\frac{(T\dot{\varphi}_{1j}^s)^2}{24}. \end{aligned} \quad (18)$$

We would like to point out that this approach is valid for higher-order vibration modes as well: vibrations whose displacements can be described by n th degree polynomials of x_i result in $2n$ th degree visibility polynomials of x_i .

For our setup, we found ‘‘tilt’’ vibrations to be slow enough that a constant visibility drop $v_j^s := v_{0j}^s$ is sufficient, yielding the following model:

$$\bar{I}_{ij} = t_{ij}^f t_i (1 + v_{ij}^f v_j^s v_i \cos(\varphi_{ij}^f + \varphi_{0j}^s + x_i \varphi_{1j}^s + \varphi_i)). \quad (19)$$

In order to obtain images $\hat{t}, \hat{v}, \hat{\varphi}$ and vibration parameters $\hat{v}^s, \hat{\varphi}_0^s, \hat{\varphi}_1^s$, we fit this model to the measured intensities,

$$L(\mathbf{t}, \mathbf{v}, \boldsymbol{\varphi}, \mathbf{v}^s, \boldsymbol{\varphi}_0^s, \boldsymbol{\varphi}_1^s) = \sum_{i,j} l(I_{ij} | \bar{I}_{ij}), \quad (20)$$

$$\{\hat{t}, \hat{v}, \hat{\varphi}, \hat{v}^s, \hat{\varphi}_0^s, \hat{\varphi}_1^s\} = \underset{\mathbf{t}, \mathbf{v}, \boldsymbol{\varphi}, \mathbf{v}^s, \boldsymbol{\varphi}_0^s, \boldsymbol{\varphi}_1^s}{\text{arg min}} L. \quad (21)$$

Notably, the solution is not unique. For any choice of $\boldsymbol{\lambda} \in \mathbb{R}^3$, $\lambda_0 \neq 0$,

$$\left\{ \begin{array}{l} \hat{t}, \quad \hat{v} \cdot \lambda_0, \quad \hat{\varphi} + \lambda_1 + \lambda_2 \mathbf{x}, \\ \hat{v}^s / \lambda_0, \quad \hat{\varphi}_0^s - \lambda_1, \quad \hat{\varphi}_1^s - \lambda_2 \end{array} \right\}$$

is a valid solution of (21), since all occurrences of $\lambda_0, \lambda_1, \lambda_2$ cancel out in (19). We select one solution by requiring

$$\text{median}(\hat{\varphi}_0^s) = 0, \quad \text{median}(\hat{\varphi}_1^s) = 0, \quad \text{median}(\hat{v}^s) = 1, \quad (22)$$

assuming that there are no long-term drifts between reference and sample measurements, and that the motion in the sample scans follows the same random distribution as the one observed in the reference scans.

D. Gradient-based optimization

In order to find the most likely images $\hat{t}, \hat{v}, \hat{\varphi}$ and grating motion parameters $\hat{\varphi}^s, \hat{v}^s$, we utilize that calculating the images while keeping $\boldsymbol{\varphi}^s, \mathbf{v}^s$ constant is computationally cheap. We define a new cost function \hat{L} where this part of the optimization has already been done,

$$\hat{L}(\mathbf{v}^s, \boldsymbol{\varphi}_0^s, \boldsymbol{\varphi}_1^s) = \min_{\mathbf{t}, \mathbf{v}, \boldsymbol{\varphi}} L = \sum_i \min_{t_i, v_i, \varphi_i} \sum_j l(I_{ij} | \bar{I}_{ij}), \quad (23)$$

$$(\hat{t}, \hat{v}, \hat{\varphi}) = \underset{\mathbf{t}, \mathbf{v}, \boldsymbol{\varphi}}{\text{arg min}} L. \quad (24)$$

As per the multivariable chain rule, its gradient is given by ($\boldsymbol{\xi}^s$ being $\mathbf{v}^s, \boldsymbol{\varphi}_0^s$ or $\boldsymbol{\varphi}_1^s$)

$$\begin{aligned} \frac{d\hat{L}}{d\boldsymbol{\xi}_j^s} &= \frac{\partial \hat{L}}{\partial \boldsymbol{\xi}_j^s} + \sum_i \left(\frac{\partial \hat{L}}{\partial t_i} \frac{\partial t_i}{\partial \boldsymbol{\xi}_j^s} + \frac{\partial \hat{L}}{\partial v_i} \frac{\partial v_i}{\partial \boldsymbol{\xi}_j^s} + \frac{\partial \hat{L}}{\partial \varphi_i} \frac{\partial \varphi_i}{\partial \boldsymbol{\xi}_j^s} \right) \\ &= \left. \frac{\partial \hat{L}}{\partial \boldsymbol{\xi}_j^s} \right|_{(\mathbf{t}, \boldsymbol{\varphi}, \mathbf{v}) = (\hat{t}, \hat{\varphi}, \hat{v})}, \end{aligned} \quad (25)$$

since $\partial \hat{L} / \partial \hat{t} = \partial \hat{L} / \partial \hat{\varphi} = \partial \hat{L} / \partial \hat{v} = \mathbf{0}$. Conveniently, this corresponds to first calculating the image and then taking the partial derivatives of the log-likelihood with respect to vibration parameters. \hat{L} is minimized using the L-BFGS algorithm [29], [30].

1) *Subsampling*: In order to increase performance, we may take only a subset of all pixels into account. Using only every n th detector column is approx. n times faster. This is similar to assuming a detector that is just $1/n$ as wide as the actual one. We found that e.g. $n = 20$ does not visibly alter the resulting images.

There are two limitations to subsampling: First, aliasing needs to be avoided: the value of the subsampled cost function does not change when substituting one of the tilt displacements φ_{1j}^s by $\varphi_{1j}^s + w/n \cdot 2\pi$, w being the number of pixels in one detector row, which is not the case for the full cost function. Second, the estimation becomes more noisy, since it is fitted to less measured data.

2) *Preconditioning*: For faster convergence, we aim to rescale the problem so that the diagonal of its Hessian is approximately one. The diagonal of the Hessian of \hat{L} is given by

$$\frac{d^2 \hat{L}}{d\boldsymbol{\xi}_j^s{}^2} = \frac{\partial^2 \hat{L}}{\partial \boldsymbol{\xi}_j^s{}^2} + \sum_i \sum_{\zeta_i \in \{t_i, v_i, \varphi_i\}} \frac{\partial^2 \hat{L}}{\partial \boldsymbol{\xi}_j^s \partial \zeta_i} \frac{\partial \zeta_i}{\partial \boldsymbol{\xi}_j^s}. \quad (26)$$

We will neglect everything but the leading term on the right side. The accuracy of this approximation can be checked empirically for a specific setup, but may be motivated by the fact that in the limit of many exposures contributing to each pixel, the dependency of the images on one single exposure's parameter $\partial \hat{L} / \partial \boldsymbol{\xi}_j^s$ vanishes. Furthermore, we approximate this expression by its statistical expectation value $\langle \cdot \rangle$ (w.r.t. the photon statistics) to obtain an expression akin to the Fisher information in standard phase retrieval [31],

$$\begin{aligned} \frac{d^2 \hat{L}}{d\boldsymbol{\xi}_j^s{}^2} &\approx \frac{\partial^2 L}{\partial \boldsymbol{\xi}_j^s{}^2} \approx \left\langle \frac{\partial^2 L}{\partial \boldsymbol{\xi}_j^s{}^2} \right\rangle = \left\langle \frac{\partial}{\partial \boldsymbol{\xi}_j^s} \sum_i \frac{\partial L}{\partial \bar{I}_{ij}} \frac{\partial \bar{I}_{ij}}{\partial \boldsymbol{\xi}_j^s} \right\rangle \\ &= \sum_i \left\langle \frac{\partial L}{\partial \bar{I}_{ij}} \right\rangle \frac{\partial^2 \bar{I}_{ij}}{\partial \boldsymbol{\xi}_j^s{}^2} + \sum_i \left\langle \frac{\partial^2 L}{\partial \bar{I}_{ij}^2} \right\rangle \left(\frac{\partial \bar{I}_{ij}}{\partial \boldsymbol{\xi}_j^s} \right)^2 \\ &\approx \sum_i \frac{2}{\bar{I}_{ij}} \left(\frac{\partial \bar{I}_{ij}}{\partial \boldsymbol{\xi}_j^s} \right)^2, \end{aligned} \quad (27)$$

since

$$\left\langle \frac{\partial L}{\partial \bar{I}_{ij}} \right\rangle = \left\langle \frac{2(\bar{I}_{ij} - I_{ij})}{\bar{I}_{ij}} \right\rangle \approx 0, \quad (28)$$

$$\left\langle \frac{\partial^2 L}{\partial \bar{I}_{ij}^2} \right\rangle \approx \frac{2}{\bar{I}_{ij}}. \quad (29)$$

TABLE I
MATERIAL PARAMETERS OF THE PHANTOM STUDY

	μ (1/mm)	δ (1/mm)	ϵ (1/mm)
1 Lung	$6.35 \cdot 10^{-3}$	$5.90 \cdot 10^{-3}$	$6.49 \cdot 10^{-3}$
2 Soft tissue	$2.58 \cdot 10^{-2}$	$2.41 \cdot 10^{-2}$	0
3 Bone marrow	$2.18 \cdot 10^{-2}$	$2.07 \cdot 10^{-2}$	0
4 Bone	$9.96 \cdot 10^{-2}$	$8.14 \cdot 10^{-2}$	0

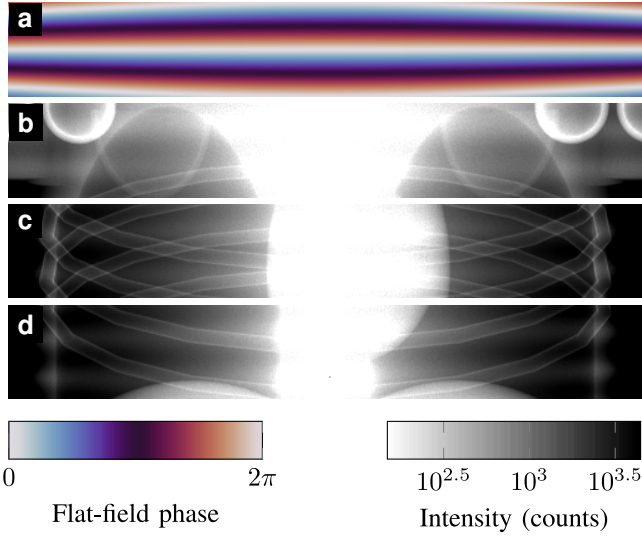


Fig. 3. Simulation study. The flat-field phase of one exposure is shown in (a). Raw measurements of the phantom were simulated, of which (b-d) depict three exemplary ones (positions in scan 52, 104, and 156).

To obtain an estimate that depends less on the initial guess, we take the average over all possible grating positions, neglect the influence of motion during the exposure ($v^s \approx 1$) and obtain

$$\frac{d^2 \hat{L}}{d\varphi_{0j}^s{}^2} \approx \frac{1}{\pi} \sum_i t_{ij}^f \hat{t}_i (v_{ij}^f \hat{v}_i)^2 \int_0^{2\pi} \frac{\sin^2 \varphi}{1 + v_{ij}^f \hat{v}_i \cos \varphi} d\varphi. \quad (30)$$

Expanding this expression and similar ones for the remaining variables up to the vanishing third order in $v_{ij}^f \hat{v}_i$ yields:

$$\frac{d^2 \hat{L}}{d\varphi_{0j}^s{}^2} \approx \sum_i t_{ij}^f \hat{t}_i (v_{ij}^f \hat{v}_i)^2 =: h_{\varphi 0j}, \quad (31)$$

$$\frac{d^2 \hat{L}}{d\varphi_{1j}^s{}^2} \approx \sum_i t_{ij}^f \hat{t}_i (v_{ij}^f \hat{v}_i)^2 x_i^2 =: h_{\varphi 1j}, \quad (32)$$

$$\frac{d^2 \hat{L}}{dv_j^s{}^2} \approx \sum_i t_{ij}^f \hat{t}_i (v_{ij}^f \hat{v}_i)^2 =: h_{vj}. \quad (33)$$

This can be used to rescale the problem so that the diagonal of its Hessian is nearly constant. I.e., instead of \hat{L} , we optimize

$$\hat{M}(\tilde{\varphi}_0^s, \tilde{\varphi}_1^s, \tilde{v}^s) := \hat{L} \left(\tilde{\varphi}_0^s \odot (h_{\varphi 0})^{\circ \frac{1}{2}}, \tilde{\varphi}_1^s \odot (h_{\varphi 1})^{\circ \frac{1}{2}}, \tilde{v}^s \odot (h_v)^{\circ \frac{1}{2}} \right), \quad (34)$$

where \odot and $\circ^{\frac{1}{2}}$ denote the element-wise division and square root, respectively.

E. Dealing with sample motion and non-convexity

If the sample or a part of it is moving during acquisition, which is inevitably the case for a human patient and the relatively long acquisition time of a scanning setup, the algorithm described above falsely attributes that inconsistent transmission data to grating motion, often resulting in strong additional artifacts. This is mitigated by excluding pixels subject to motion, which can be identified by examining the “intensity-normalized” residual $\hat{\epsilon}_i$ for each detector pixel,

$$\hat{\epsilon}_i = \min_{t_i, v_i, \varphi_i} \sum_j l(I_{ij} | \bar{I}_{ij}), \quad (35)$$

before starting the optimization: if the transmission in said pixel is inconsistent, the stepping curve is no longer a good model for the measured intensities and $\hat{\epsilon}_i$ becomes large. Thus, pixels where $\hat{\epsilon}_i$ exceeds some empirically established threshold are excluded. We note that this choice is not crucial: discarding some pixels that are not actually subject to motion will not have a significant influence on the outcome, as long as enough pixels of each shot are assumed to be valid. We take advantage of the same redundancy in Sec. II-D when taking only a subset of the detector’s columns into account. After determining the vibration parameters, the final images are retrieved taking all pixels into account.

The optimization problem stated in (21) is non-convex. We found a combination of two measures suitable to avoid local minima: First, we replace the phase image by its circular mean during the first iterations:

$$\varphi \leftarrow \mathbf{1} \cdot \text{circmean}(\varphi), \quad (36)$$

$$\text{circmean}(\varphi) := \arg \left(\sum_k \exp(i\varphi_k) \right). \quad (37)$$

This is similar to setting the transmission to unity in [32]. Second, we start by optimizing φ^s , and add v^s to the optimization problem when φ^s has already mostly converged.

F. Inapplicability of the algorithm to a stepping acquisition scheme

For a phase stepping acquisition scheme, there is no unique solution when optimizing for per-exposure phase and visibility. Suppose we found the correct solution locally minimizing the log-likelihood. Then, the model intensities \hat{I}_{ij} fitting the data optimally are given by

$$\hat{I}_{ij} = \hat{t}_i (1 + \hat{v}_j^s \hat{v}_i \cos(\hat{\varphi}_j^s + \hat{\varphi}_i)). \quad (38)$$

The key difference to (19) is that the flat field does not change from exposure to exposure. Hence, unlike for inhomogeneous gratings used in a scanning acquisition scheme, distinguishing between sample and flat field is not necessary. Just like in (8), per-exposure and per-pixel quantities can be separated:

$$\begin{aligned} \hat{I}_{ij} &= \hat{t}_i (1 + \hat{v}_j^s \hat{v}_i (\cos \hat{\varphi}_j^s \cos \hat{\varphi}_i - \sin \hat{\varphi}_j^s \sin \hat{\varphi}_i)) \\ &= \hat{t}_i + \hat{v}_j^s \cos \hat{\varphi}_j^s \cdot \hat{t}_i \hat{v}_i \cos \hat{\varphi}_i - \hat{v}_j^s \sin \hat{\varphi}_j^s \cdot \hat{t}_i \hat{v}_i \sin \hat{\varphi}_i. \end{aligned} \quad (39)$$

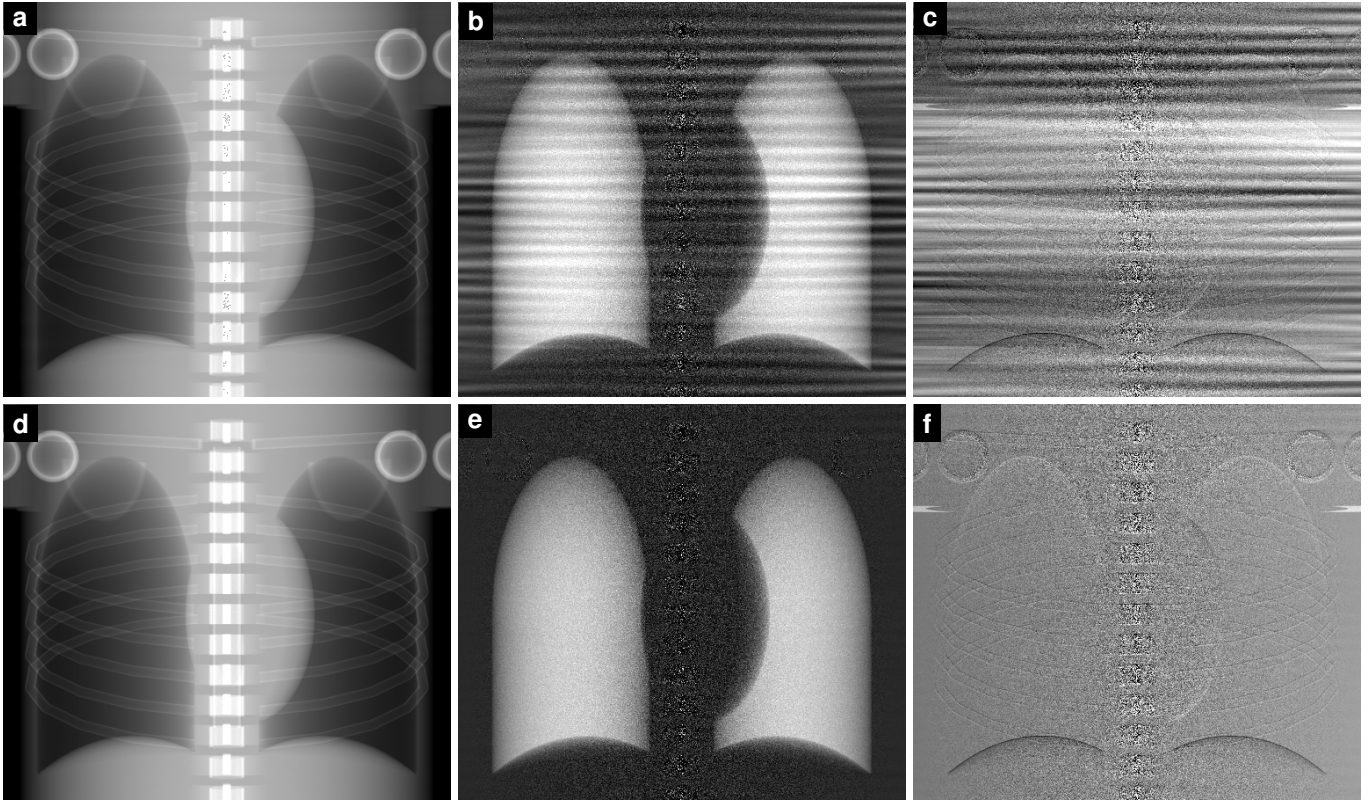


Fig. 4. Results of the simulation study. Retrieved attenuation (a, d), dark-field (b, e), and differential phase (c, f) images before (a–c) and after (d–f) estimation of grating vibrations. The grayscales are as in Fig. 2.

By a change of variables,

$$\begin{aligned} \hat{c}_j^s &:= \hat{v}_j^s \cos \hat{\varphi}_j^s, & \hat{s}_j^s &:= \hat{v}_j^s \sin \hat{\varphi}_j^s, \\ \hat{c}_i &:= \hat{t}_i \hat{v}_i \cos \hat{\varphi}_i, & \hat{s}_i &:= \hat{t}_i \hat{v}_i \sin \hat{\varphi}_i, \end{aligned} \quad (40)$$

we obtain an equivalent linear equation,

$$\hat{I}_{ij} = \hat{t}_i + \hat{c}_j^s \cdot \hat{c}_i - \hat{s}_j^s \cdot \hat{s}_i. \quad (41)$$

We can construct many different solutions \bullet' that fit the data just as well, e.g. these ones, parameterized by $\lambda \in \mathbb{R}$:

$$\hat{c}^{s'} = \hat{c}^s + \lambda, \quad (42)$$

$$\hat{t}' = \hat{t} - \lambda \hat{c} \quad (43)$$

$$\Rightarrow \hat{I}'_{ij} = (\hat{t}_i - \lambda \hat{c}_i) + \hat{c}_i (\hat{c}_j^s + \lambda) - \hat{s}_j^s \hat{s}_i = \hat{I}_{ij}. \quad (44)$$

To illustrate these spurious solutions, we obtain expressions for the resulting images by applying (10):

$$\hat{t}'_i = \hat{t}_i (1 - \lambda \hat{v}_i \cos(\hat{\varphi}_i)), \quad (45)$$

$$\hat{\varphi}'_i = \hat{\varphi}_i, \quad (46)$$

$$\hat{v}'_i = (1 - \lambda \hat{v}_i \cos \hat{\varphi}_i)^{-1} \hat{v}_i. \quad (47)$$

Thus, this kind of optimization scheme is not suitable for stepped data when grating motion *during* exposures is taken into account. This is also the case for flat fields in scanning setups, which are measured in a stepping acquisition scheme.

In theory, this situation also occurs in a perfectly uniform scanning interferometer, when t_{ij}^f and v_{ij}^f are independent of j ,

and the flat-field phase is separable,

$$\varphi_{ij}^f =: \beta_i + \gamma_j. \quad (48)$$

The latter is the case if the flat-field phase gradient in scanning direction is constant. In practice, this is unlikely and may easily be avoided by detuning the interferometer slightly.

III. RESULTS

A. Simulation study

We conceived a simulation study for a scanning X-ray Talbot-Lau interferometer affected by mechanical vibrations roughly resembling the clinical prototype. The simulation is monochromatic at an energy of 45 keV. The distance from source to the patient centre is 1.5 m, the distance from source to detector is 1.8 m. We assume a detector having 1 mm × 1 mm pixels, with a total size of 45 cm × 51 cm, resulting in a field of view of 37.5 cm × 42.5 cm.

The interferometer features horizontal grating lines, and has characteristic parameters $c_v = 1$, $c_\varphi = 40 \mu\text{m}$ and a spatially constant flat-field visibility $v^f = 0.3$ and illumination $t^f = 2 \cdot 10^4$ photons. The active area of the interferometer is 7.5 cm high and as wide as the detector. There are two moiré fringes in the center, and 2.5 moiré fringes at the left and the right edge of the grating. The active area moves 0.25 cm in between two exposures and traverses the entire detector, resulting in 30 exposures of each detector pixel, and 209 exposures in total.

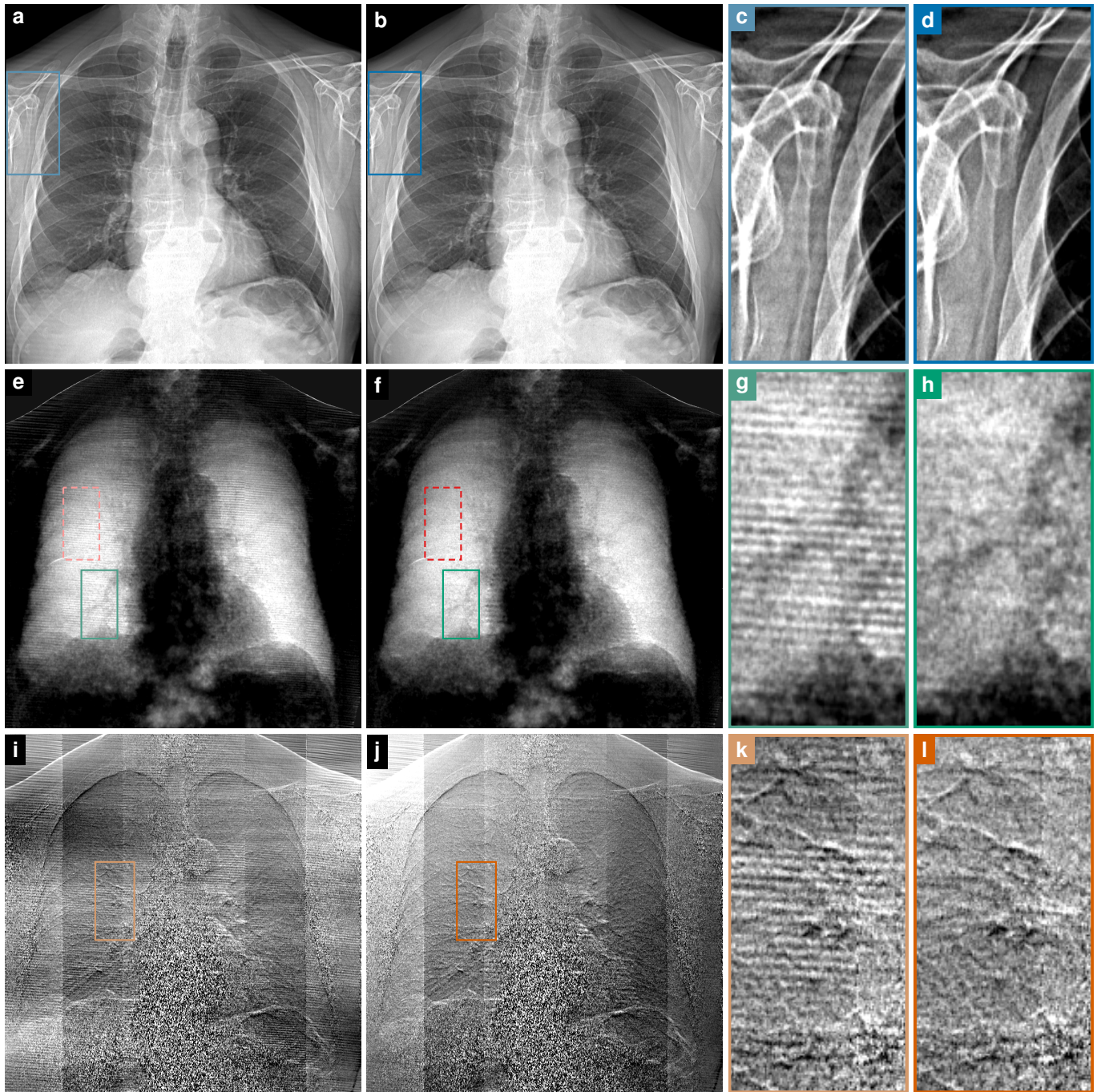


Fig. 5. Correction of vibration artefacts in images of a patient's thorax (77 year old male). Retrieved attenuation (a–d), dark-field (e–h) and differential phase images before (first column) and after (second column) estimation of grating vibrations. The third and the fourth column show zoom-ins of the uncorrected and corrected images, respectively. Zoom-ins of the dashed regions are shown in Fig. 7. For the logarithmic dark-field images, a window from $-\ln 1.05$ to $-\ln 0.55$ was chosen, for the differential phase images, it ranges from -0.2 to 0.2 . The zoom-ins feature narrower windows. The scan was performed at 70 kVp, with a total scan duration of 7 s, and an estimated effective dose [33] of $43 \mu\text{Sv}$. The field of view is $37 \text{ cm} \times 37 \text{ cm}$.

The phantom is the FORBILD thorax phantom [34], extended by a refractive index decrement and a dark-field material property, i.e. linear diffusion coefficient. Fig. 2 shows the phantom data. Assumed material parameters are given in Table I, which were calculated from [35] except ϵ , whose choice is motivated by the values typically found in images of patients. The flat-field phase and three exemplary raw images are displayed in Fig. 3.

Simulating mechanical vibrations, φ_{0j}^s and φ_{1j}^s were drawn from a normal distribution with $\mu_\varphi = 0$, $\sigma_\varphi = 2\pi/16$. The flat fields are assumed to be known exactly, i.e. contain neither noise nor vibrations. The visibility reduction v^s due to motion was calculated by $|1 - |u||$, where u was drawn from a normal distribution with $\mu_u = 0$, $\sigma_u = 0.2$. This choice corresponds to vibrations that are approximately twice as large as what we observe experimentally. The probability distribution of v^s was chosen to avoid negative visibilities, which are physically impossible, as well as visibilities larger than one: due to the choice of perfect flat fields, vibrations in the sample scan will always result in a visibility reduction. In the reconstruction, we assume $\max(\hat{v}^s) = 1$ accordingly.

Fig. 4 shows the resulting images before and after applying the proposed algorithm. Even without correction, there are no visible artifacts in the transmission image for these simulation parameters. The uncorrected dark-field image is not only impaired by fringe-like artifacts, it is also quantitatively wrong, since the vibration-induced loss of fringe visibility is falsely interpreted as a dark-field signal. All visible artifacts from vibrations are successfully removed, both in the dark-field and in the differential phase image. A slight global ramp in x direction is visible in the corrected differential phase image, due to the ambiguity mentioned in Sec. II-C.

B. Experimental validation

After a first validation in simulations, we applied the algorithm to a real scan of a patient. The setup is the one described in [9], a scanning-type Talbot-Lau interferometer with horizontal grating lines and an active area of $42\text{ cm} \times 6.5\text{ cm}$, which is moved in vertical direction to reach a total field of view of $42\text{ cm} \times 42\text{ cm}$ measured in the detector plane. One scan takes 7s, while acquiring 195 partially overlapping frames, resulting in at least 24 exposures of each detector pixel. Raw images are recorded using a flat-panel detector; the rotating anode X-ray source is operated at 70 kVp. Regardless of whether the vibration correction has been applied, the images are corrected for the effects of Compton scatter, beam-hardening, and dark-field bias [36] in regions with particularly low transmission. Adapted Unique processing (Unique X-ray image processing software, Philips Healthcare, The Netherlands) was applied to attenuation images to obtain an appearance akin to regular chest X-ray images [37]. The dark-field image has been iteratively denoised to achieve spatially constant noise variance [38]. The resulting images with and without vibration correction are shown in Fig. 5. Unlike in the simulation study, even the attenuation image exhibits some faint, yet visible fringe artifacts. Most artifacts in all three images are successfully removed; we attribute residual artifacts

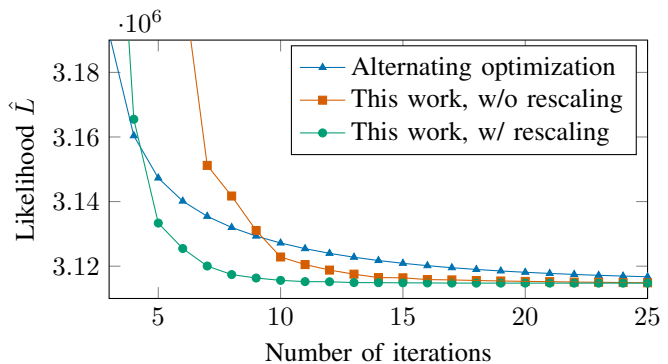


Fig. 6. Comparison of convergence speed of our novel algorithm with the alternating optimization one used in [18], [20].

close to the heart, which feature a different spatial frequency, to cardiac motion. In [39], we provide a detailed description of their formation and an algorithm for their reduction. Some of the residual artefacts at the right shoulder are presumably caused by patient motion as well, as this area features large gradients of the transmission. Besides, residual Compton scatter would impair this particular area strongly as well, since the illuminated area of the sample is changing particularly quickly. There are phase ramps with discontinuities at the boundaries of the G_2 grating's tiles, which are present in the uncorrected as well as in the corrected images. These are caused by a single random vertical offset of the whole interferometer during the sample scan with respect to the reference scans. Because the vertical gradient of the flat-field phase is discontinuous at the grating boundaries, the effect is most striking there. Removing these artefacts is beyond the scope of this paper.

C. Evaluation of the convergence rate

Here, we demonstrate that our method outperforms alternating minimization of the same loglikelihood [20], [21] in scanning setups, and that the preconditioning described in Sec. II-D.2 is effective.

In order to enable a performance-only comparison with the previous algorithms as originally presented, we simulated and reconstructed only linear displacements in between exposures ($\varphi_1^s = 0$, $v^s = 1$). All other parameters of the simulated measurement were the same as before. For our method, we omitted the subsampling described in Sec. II-D as well as the measures to avoid local minima sketched in Sec. II-E. Further, we included an evaluation of the effect of rescaling the per-shot parameters in our model.

Since both methods involve a similar computational effort for each iteration, we compared the convergence rate by number of iterations, see Fig. 6. Except for very early iterations, our method converges faster than alternating optimization approaches, and rescaling the problem clearly accelerates convergence.

The algorithm presented in [22] comprises an extension of the one in [20] by rotational vibrations at the expense of replacing the formerly accurate optimization step of the per-shot parameters by an approximation. Thus, we expect a behaviour similar to [20] at best. We are not aware of a

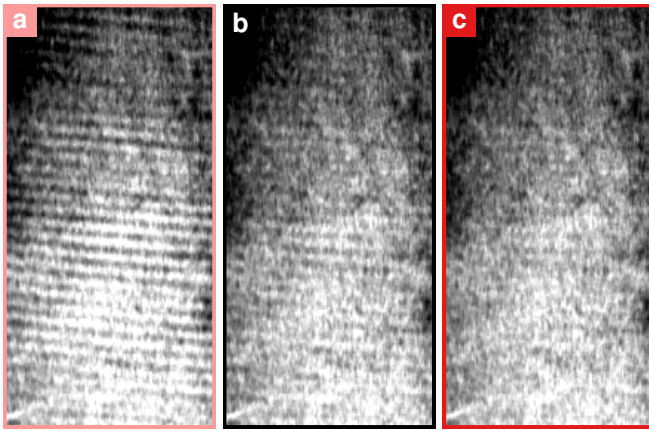


Fig. 7. The effect on the dark-field image of modelling motion during exposures (c) compared with correcting only motion between exposures (b) and no correction at all (a). The region for these zoom-ins is marked in Fig. 5.

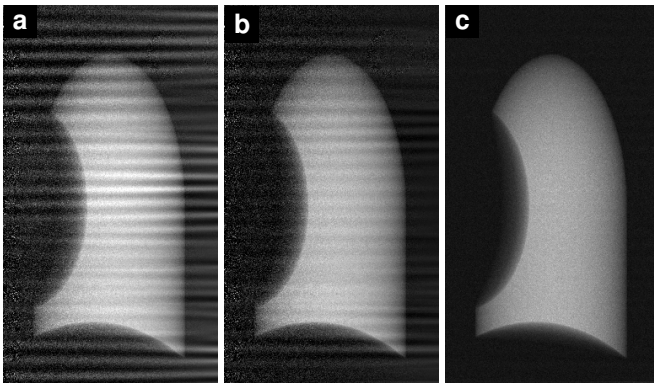


Fig. 8. Evaluation of the performance of the algorithm presented in [18] when reconstructing our computational phantom. (a) uncorrected image, (b) corrected image, (c) corrected image, this time using a spatially constant attenuation image. The grayscales are as in Fig. 4.

possible generalization of the initial PCA step in [21] or of the algorithm presented in [23] that can be applied to scanned datasets.

D. Comparison with other algorithms by image quality

1) *Motion during exposures*: None of the methods prior to this work considers motion during exposures. To assess the effect of this new feature on our images, we repeated the study from Sec. III-B, but this time excluding v^s from the fit. Fig. 7 displays the result of this approach. While the majority of the artefacts originates from grating displacement and rotation between exposures, there is a distinct amount of artefacts rising from motion-induced visibility loss. The transmission and differential phase images are not shown, because they do not show a clear change in image quality.

2) *Comparison against a previous method for images acquired by scanning*: The method described in [18] deserves a closer examination, since it is to our knowledge the first and so far only attempt to correct grating instabilities in a scanning setup. In short, they assume random grating displacements up to second order in x , which is equal to our model (19)

extended by an additional quadratic term $x_i^2 \varphi_{ij}^s$. Their model does not include vibration-induced visibility loss, which might not occur in that setup in the first place. However, the vibration parameters are obtained in an entirely different way: For a range of different grating positions, virtual intensity patterns for the unloaded interferometer are calculated from the flat field. Then, column-wise grating positions are determined so that they maximize the correlation between the actually measured intensities and these simulated fringe patterns. Then, for each exposure, the authors fit a polynomial to these column-wise grating positions. Because the correlations are generally distorted in presence of a sample, in particular by the sample's transmission, a robust fit is chosen for this step, which helps dealing with these transmission-induced “outliers”.

When evaluating this algorithm using our simulated measurements, we did not simulate any motion-induced visibility reduction to allow for a more instructive comparison. Also, the quadratic term in the fit was omitted, since the synthetic data does not feature such a mode. The scaling parameter of the bisquare loss function was chosen empirically. The results are displayed in Fig. 8. Due to the correlations between the sample's transmission and the fringe pattern, the algorithm can not accurately retrieve the grating positions in our simulation. To illustrate this effect further, we varied the simulation, this time using a constant attenuation image for raw data simulation. Since there is no correlation between the fringe pattern and the sample's transmission in this setting, the reconstruction is flawless.

In real patient images, we found that the performance of the algorithm varies considerably from image to image. While in some cases, the results look similar to our ones, some images are reconstructed considerably worse, see Fig. 9 for one example.

3) *Reproducibility of measurements*: Because one random contributing factor is eliminated, grating vibration estimation is supposed to increase the reproducibility of measurements. To examine this feature, we carried out 32 measurements of the Multipurpose Chest Phantom N1 “LUNGMAN” (Kyoto Kagaku, Kyoto, Japan). It resembles a human thorax at least in terms of transmission; the dark-field image shows spurious signal from the bones, which is much stronger than the signal observed from real lung tissue, and lacks realistic signal from the lungs. In Fig. 10, we compare the dark-field images computed from the initial scan against the average of the images from all 32 scans, using different processing methods. While both our method and the one described in [18] constitute a clear improvement against no modelling of vibrations at all, their differences are more subtle. We argue that a quantitative comparison using phantom scans is tricky, since the variations are dominated by photon shot noise and detector noise. This is also why the deviations are smaller in the area of the lung, which features a higher transmission than the surrounding area. Moreover, noise propagation through phase retrieval is influenced by the assumed vibration parameters. More precisely, correctly guessing a reduced visibility increases the noise in the retrieved dark-field image.

4) *Noise power spectra of blank scans*: To overcome the shortcomings of the measurements above and to provide a

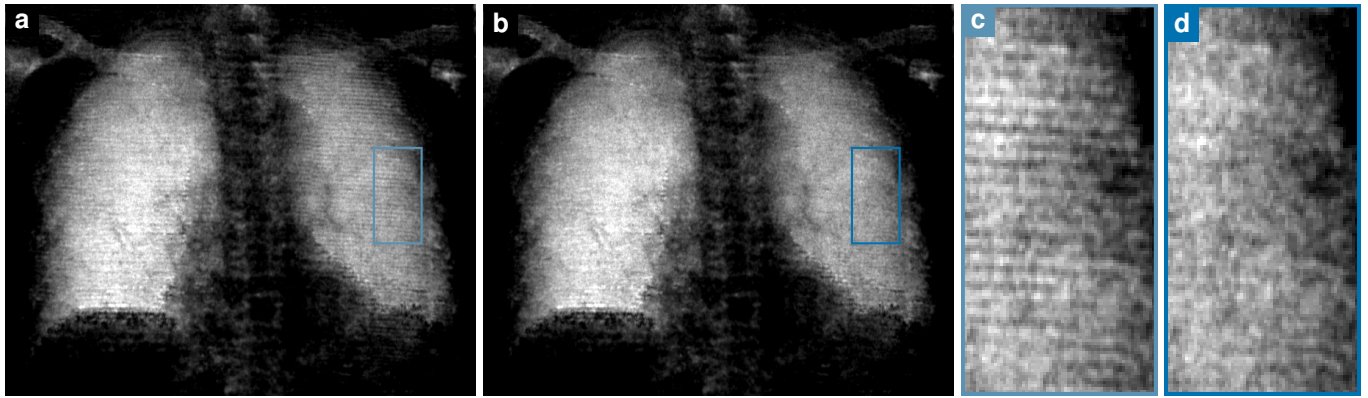


Fig. 9. Dark-field image of a patient's thorax (54 year old female, infected with COVID-19), corrected for grating vibration using (a, zoom-in c) the algorithm described in [18] and (b, zoom-in d) our algorithm. The window of the dark-field images is $-\ln 1$ to $-\ln 0.62$. The zoom-ins feature narrower windows.

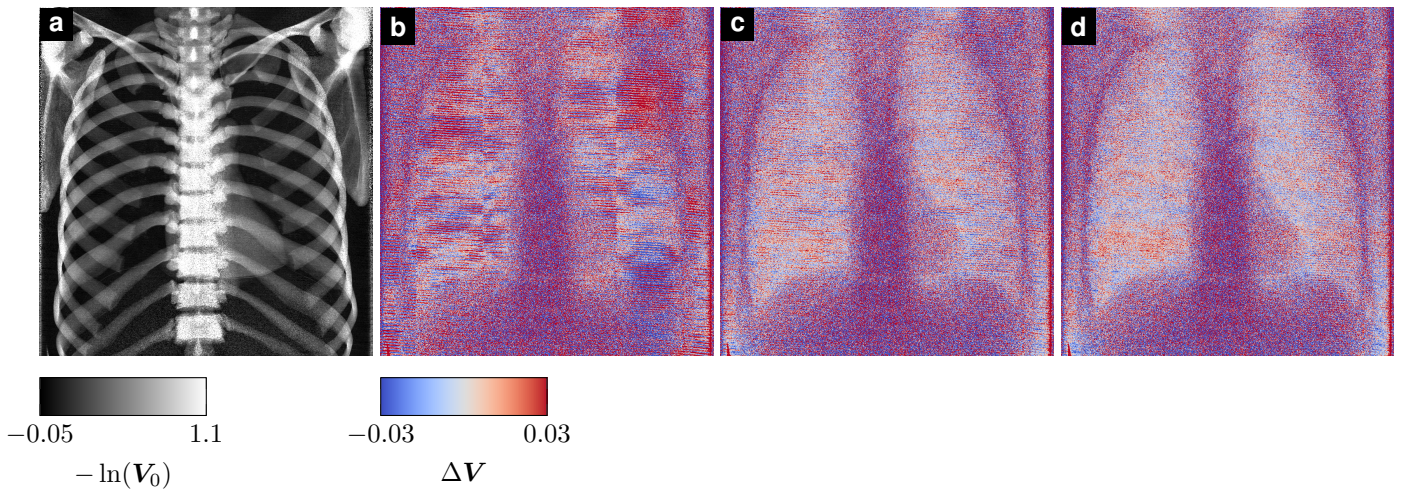


Fig. 10. Reproducibility of measurements in a phantom with human-like transmission properties. (a) exemplary dark-field image, (b–d) difference $\Delta V = V_0 - 1/32 \sum_{i=0}^{31} V_i$ between the first one of 32 dark-field images taken in consecutive scans and their average, processed using (b) no correction for vibrations at all, (c) algorithm [18], (a, d) this work.

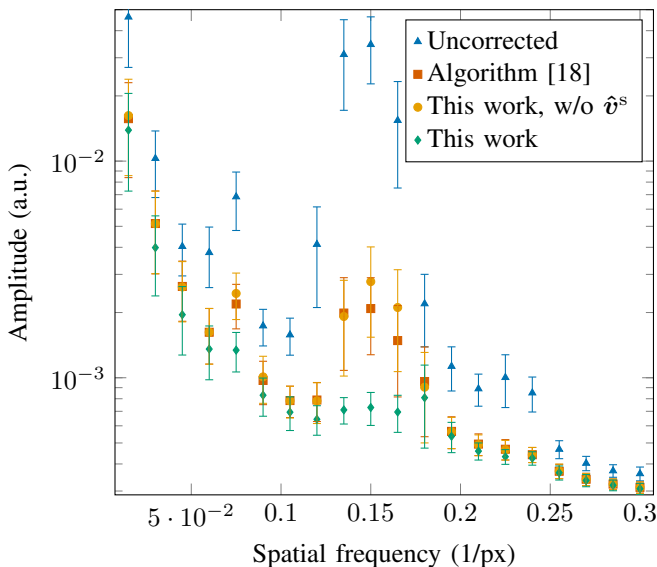


Fig. 11. Binned radial noise power spectra of empty dark-field images, processed using different algorithms. The error bars mark one standard deviation.

quantitative analysis, we analyzed noise power spectra of dark-field images. Ideally, these would be taken from sample-free areas of patient images. However, these are very small due to careful collimation, and often overexposed. Instead, we utilized empty scans. These scans were acquired after each of the patient scans from the study in [9], respectively; here, we take the first 50 of these into account. By separating the whole image into its spatial frequencies, we can focus on the ones associated with vibrations - namely the fringe frequency and its first harmonic [15]. These noise power spectra are displayed in Fig. 11. As can be seen, our method works reliably and removes a much larger fraction of fringe artefacts than the one presented in [18]. The artefacts' spatial frequency is consistent with our fringe size of about 14 px.

IV. DISCUSSION AND CONCLUSION

We propose an algorithm for correcting artifacts due to grating motion occurring both during and between exposures. We first demonstrated its functionality on simulated data, and then successfully applied it to data from a state-of-the-art

scanning Talbot-Lau interferometer. While this kind of setup is generally more prone to vibrations than static setups, it turns out that motion both in between and during exposures can be accounted for. Because the algorithm is formulated as an extension of standard least-squares phase retrieval, implementation is straightforward. These findings may lead to more relaxed stability constraints, and thus, easier construction of future interferometers. While processing becomes much more robust, this approach still has some requirements on setup stability, namely uniform motion of small amplitude during exposures. It has to be noted that while motion-induced bias can be avoided, random grating positions and randomly reduced visibility still result in an increased noise level that is not even spatially homogeneous.

Most recently, an alternative large animal scanning system was presented [40] where the pig is moved through a stationary interferometer. While this avoids vibrations, it suffers from additional artifacts due to sample motion. More importantly, this concept seems impractical for patient imaging in upright position, which is the preferred acquisition setup for chest radiography.

Because our method builds solely upon a stochastic model for the measured intensities, effects that are not included in the model must be corrected for beforehand. In our case, these are motion of the sample and Compton scatter. Compton scatter can be estimated; regions affected by motion can be excluded from the optimization problem. Unlike in this work, the source spot is not fixed with respect to the sample in most scanning setups. In that case, the beam paths (2)–(4) for the same pixel change slightly during the scanning process, so there is additional inconsistency in the measured intensities. Future research will show to what extent the presented algorithm is compatible with that approximation.

ACKNOWLEDGMENT

We acknowledge Hendrik van der Heijden, Karsten Rindt, Jens von Berg, Sven Prevrhal, Roland Proksa, Michael Heider, Andre Yaroshenko, and Thomas Pralow gratefully for assistance during the hardware and software development for the demonstrator system, and Florian Schaff, Detlef Mentrup, Clemens Schmid and Andre Yaroshenko for helpful comments on the manuscript.

REFERENCES

- [1] A. Lohmann and D. Silva, "An interferometer based on the Talbot effect," *Opt. Commun.*, vol. 2, no. 9, pp. 413–415, 1971.
- [2] S. Yokozeki and T. Suzuki, "Shearing interferometer using the grating as the beam splitter," *Appl. Opt.*, vol. 10, no. 7, pp. 1575–1580, 1971.
- [3] A. Momose, S. Kawamoto, I. Koyama, Y. Hamaishi, K. Takai, and Y. Suzuki, "Demonstration of X-ray Talbot interferometry," *Jpn. J. Appl. Phys., Part 2*, vol. 42, no. 7B, pp. L866–L868, 2003.
- [4] F. Pfeiffer, T. Weitkamp, O. Bunk, and C. David, "Phase retrieval and differential phase-contrast imaging with low-brilliance X-ray sources," *Nat. Phys.*, vol. 2, no. 4, pp. 258–261, 2006.

- [5] F. Pfeiffer *et al.*, "Hard-X-ray dark-field imaging using a grating interferometer," *Nat. Mater.*, vol. 7, no. 2, pp. 134–137, 2008.
- [6] J. Tanaka *et al.*, "Cadaveric and in vivo human joint imaging based on differential phase contrast by X-ray Talbot-Lau interferometry," *Z. Med. Phys.*, vol. 23, no. 3, pp. 222–227, 2013.
- [7] L. B. Gromann *et al.*, "In-vivo X-ray dark-field chest radiography of a pig," *Sci. Rep.*, vol. 7, 4807, 2017.
- [8] K. Willer *et al.*, "X-ray dark-field imaging of the human lung—a feasibility study on a deceased body," *PLOS ONE*, vol. 13, no. 9, e0204565, 2018.
- [9] K. Willer *et al.*, "X-ray dark-field chest imaging for detection and quantification of emphysema in patients with chronic obstructive pulmonary disease: A diagnostic accuracy study," *Lancet Digit. Health*, vol. 3, no. 11, e733–e744, 2021.
- [10] C. Kottler, F. Pfeiffer, O. Bunk, C. Grünzweig, and C. David, "Grating interferometer based scanning setup for hard X-ray phase contrast imaging," *Rev. Sci. Instrum.*, vol. 78, no. 4, 043710, 2007.
- [11] T. Koehler *et al.*, "Slit-scanning differential X-ray phase-contrast mammography: Proof-of-concept experimental studies," *Med. Phys.*, vol. 42, no. 4, pp. 1959–1965, 2015.
- [12] J. Chen *et al.*, "Automatic image-domain moiré artifact reduction method in grating-based x-ray interferometry imaging," *Phys. Med. Biol.*, vol. 64, no. 19, 195013, 2019.
- [13] J. Vargas, C. Sorzano, J. Estrada, and J. Carazo, "Generalization of the principal component analysis algorithm for interferometry," *Opt. Commun.*, vol. 286, pp. 130–134, 2013.
- [14] G. Pelzer *et al.*, "Reconstruction method for grating-based X-ray phase-contrast images without knowledge of the grating positions," *J. Instrum.*, vol. 10, no. 12, P12017–P12017, 2015.
- [15] F. De Marco, M. Marschner, L. Birnbacher, P. Noël, J. Herzen, and F. Pfeiffer, "Analysis and correction of bias induced by phase stepping jitter in grating-based X-ray phase-contrast imaging," *Opt. Express*, vol. 26, no. 10, pp. 12 707–12 722, 2018.
- [16] S. Kaeppler *et al.*, "Improved reconstruction of phase-stepping data for Talbot-Lau X-ray imaging," *J. Med. Imaging*, vol. 4, no. 3, 034005, 2017.
- [17] C. Hauke *et al.*, "Enhanced reconstruction algorithm for moiré artifact suppression in Talbot-Lau X-ray imaging," *Phys. Med. Biol.*, vol. 63, no. 13, 135018, 2018.
- [18] M. Seifert *et al.*, "Talbot-Lau X-ray phase-contrast setup for fast scanning of large samples," *Sci. Rep.*, vol. 9, 4199, 2019.
- [19] K. Okada, A. Sato, and J. Tsujiuchi, "Simultaneous calculation of phase distribution and scanning phase shift in phase shifting interferometry," *Opt. Commun.*, vol. 84, no. 3-4, pp. 118–124, 1991.
- [20] M. Marschner *et al.*, "Helical X-ray phase-contrast computed tomography without phase stepping," *Sci. Rep.*, vol. 6, 23953, 2016.

- [21] M. Seifert *et al.*, "Optimisation of image reconstruction for phase-contrast X-ray Talbot-Lau imaging with regard to mechanical robustness," *Phys. Med. Biol.*, vol. 61, no. 17, pp. 6441–6464, 2016.
- [22] J. Dittmann, A. Balles, and S. Zabler, "Optimization based evaluation of grating interferometric phase stepping series and analysis of mechanical setup instabilities," *J. Imaging*, vol. 4, no. 6, 77, 2018.
- [23] K. Hashimoto, H. Takano, and A. Momose, "Improved reconstruction method for phase stepping data with stepping errors and dose fluctuations," *Opt. Express*, vol. 28, no. 11, pp. 16 363–16 384, 2020.
- [24] F. Pfeiffer, C. Kottler, O. Bunk, and C. David, "Hard X-ray phase tomography with low-brilliance sources," *Phys. Rev. Lett.*, vol. 98, no. 10, 2007.
- [25] M. Bech, O. Bunk, T. Donath, R. Feidenhans'l, C. David, and F. Pfeiffer, "Quantitative X-ray dark-field computed tomography," *Phys. Med. Biol.*, vol. 55, no. 18, pp. 5529–5539, 2010.
- [26] S. K. Lynch *et al.*, "Interpretation of dark-field contrast and particle-size selectivity in grating interferometers," *Appl. Opt.*, vol. 50, no. 22, pp. 4310–4319, 2011.
- [27] C. Arboleda, Z. Wang, and M. Stampanoni, "Tilted-grating approach for scanning-mode X-ray phase contrast imaging," *Opt. Express*, vol. 22, no. 13, pp. 15 447–15 458, 2014.
- [28] T. Weber *et al.*, "Noise in x-ray grating-based phase-contrast imaging," *Med. Phys.*, vol. 38, no. 7, pp. 4133–4140, 2011.
- [29] D. C. Liu and J. Nocedal, "On the limited memory BFGS method for large scale optimization," *Math. Program.*, vol. 45, no. 1-3, pp. 503–528, 1989.
- [30] Naoaki Okazaki, *libLBFGS*, <http://www.chokkan.org/software/liblbfgs/>.
- [31] K. Mechlem, T. Sellerer, M. Viermetz, J. Herzen, and F. Pfeiffer, "A theoretical framework for comparing noise characteristics of spectral, differential phase-contrast and spectral differential phase-contrast x-ray imaging," *Phys. Med. Biol.*, vol. 65, no. 6, p. 065 010, 2020.
- [32] Z. Wang and B. Han, "Advanced iterative algorithm for phase extraction of randomly phase-shifted interferograms," *Opt. Lett.*, vol. 29, no. 14, pp. 1671–1673, 2004.
- [33] M. Frank *et al.*, "Dosimetry on first clinical dark-field chest radiography," *Med. Phys.*, in press.
- [34] K. Sourbelle, *FORBILD Thorax phantom*, <http://www.imp.uni-erlangen.de/phantoms/>, 1999.
- [35] "Report 44: Tissue substitutes in radiation dosimetry and measurement," International Commission on Radiation Units and Measurements, Bethesda, MD, Tech. Rep., 1989.
- [36] M. Chabior, T. Donath, C. David, M. Schuster, C. Schroer, and F. Pfeiffer, "Signal-to-noise ratio in X-ray dark-field imaging using a grating interferometer," *J. Appl. Phys.*, vol. 110, no. 5, p. 053 105, 2011.
- [37] M. Stahl, T. Aach, and S. Dippel, "Digital radiography enhancement by nonlinear multiscale processing," *Med. Phys.*, vol. 27, no. 1, pp. 56–65, 2000.
- [38] W. Noichl *et al.*, "Reconstruction of X-ray dark-field chest images from a scanning moiré system used in a first patient study," in *X-ray and Neutron Phase Imaging with Gratings*, 2019.
- [39] R. C. Schick *et al.*, "Correction of motion artifacts in dark-field radiography of the human chest," *Trans. Med. Imaging*, 2021.
- [40] D. H. Bushe *et al.*, "A multi-contrast chest x-ray radiography prototype with low-dose fast scanning-beam acquisition," in *Medical Imaging 2022: Physics of Medical Imaging*, W. Zhao and L. Yu, Eds., International Society for Optics and Photonics, vol. PC12031, SPIE, 2022.